

## Article

# Characteristic Differences of Thermal Runaway Triggered by Overheating and Overcharging in Lithium-Ion Batteries and Multi-Dimensional Safety Protection Strategies

Yao Yao <sup>1</sup>, Lu Liu <sup>1</sup>, Juan Gu <sup>1</sup>, Haozhe Xing <sup>1</sup>, Huachao Liu <sup>1</sup>, Yihao Cheng <sup>1</sup>, Youning Wang <sup>1</sup>, Songlin Yue <sup>1</sup>, Yanyu Qiu <sup>1</sup> and Zhi Zhang <sup>2,\*</sup>

<sup>1</sup> State Key Laboratory for Disaster Prevention & Mitigation of Explosion & Impact, Army Engineering University of PLA, Nanjing 210007, China; gujuan0617@126.com (J.G.); haozhexing@hotmail.com (H.X.); wangyouning9856@163.com (Y.W.); yslseu@hotmail.com (S.Y.); qiyanyu78@sina.com (Y.Q.)

<sup>2</sup> Position Engineering Research Office, Army Engineering University of PLA, Nanjing 210007, China

\* Correspondence: zhangnjjn@outlook.com

## Abstract

Overheating and overcharging are the core triggering conditions for the thermal runaway of lithium-ion batteries. Studying the behavioral differences of thermal runaway of lithium-ion batteries under these two conditions is crucial for the safety design and protection of lithium-ion batteries. In this study, we investigated the temperature, pressure, gas generation, and heat generation characteristics of lithium batteries under these two conditions. Under overheating conditions, the release of lattice oxygen in the cathode and the decomposition of the electrolyte trigger a self-catalytic reaction, generating CO<sub>2</sub> (54.7%) and H<sub>2</sub> (29.7%), with a total heat release of 17.6 kJ and a heat accumulation rate of 24.3 W, forming a local high-temperature core area. Under overcharging conditions, the voltage drop, capacity attenuation of 21.1% (2230→1762 mAh), and internal resistance surge (6→21 mΩ) reflect severe damage to the electrode. Accompanied by the oxygenation of the EC electrolyte (CO<sub>3</sub><sup>2-</sup> + C<sub>2</sub>H<sub>4</sub>↑), the gas production rate is faster. The middle pressure was 0.601 MPa, and the proportion of CO<sub>2</sub> was 67.4%. However, the triggering of thermal runaway relies on the synergistic effect of internal electrochemical reactions and ohmic heat accumulation, resulting in a relatively low rate of energy accumulation.

**Keywords:** lithium-ion battery; thermal runaway; overheating; overcharging



Academic Editor: Torsten Brezesinski

Received: 14 May 2025

Revised: 11 June 2025

Accepted: 22 June 2025

Published: 24 June 2025

**Citation:** Yao, Y.; Liu, L.; Gu, J.; Xing, H.; Liu, H.; Cheng, Y.; Wang, Y.; Yue, S.; Qiu, Y.; Zhang, Z. Characteristic Differences of Thermal Runaway Triggered by Overheating and Overcharging in Lithium-Ion Batteries and Multi-Dimensional Safety Protection Strategies. *Batteries* **2025**, *11*, 242. <https://doi.org/10.3390/batteries11070242>

**Copyright:** © 2025 by the authors. Licensee MDPI, Basel, Switzerland. This article is an open access article distributed under the terms and conditions of the Creative Commons Attribution (CC BY) license (<https://creativecommons.org/licenses/by/4.0/>).

## 1. Introduction

Lithium-ion batteries, renowned for their high energy density, long cycle life, and environmental friendliness, have become the core energy carriers for electric vehicles (EVs), energy storage systems, and portable electronics [1–4]. However, with the pursuit of higher energy density (e.g., the widespread adoption of ternary cathode materials like Li(NiCoMn)O<sub>2</sub>), the risk of thermal runaway (TR) has significantly increased, potentially leading to fire and explosion hazards [5–10].

Thermal runaway is typically triggered by mechanical, electrical, or thermal abuses, with overheating-induced TR (temperature > 120 °C) and overcharging-induced TR (voltage > 4.2 V) being two typical modes [11,12]. The mechanism of overheating TR involves a chain reaction: when the temperature exceeds the decomposition threshold of the solid electrolyte interphase (SEI, ~120 °C), SEI breakdown exposes the anode to electrolyte, triggering exothermic reactions ( $\Delta H > 2000 \text{ kJ/kg}$ ). Subsequent phase transitions in cathode

materials (e.g., NCM ternary cathodes shifting from layered to spinel structures) release oxygen, accelerating electrolyte oxidation and culminating in thermal runaway [13–15]. In contrast, overcharging TR arises from electrochemical imbalance: excessive charging causes lithium plating on the anode, forming dendrites that pierce the separator (<20  $\mu\text{m}$  thickness exacerbates risks), inducing internal short circuits. Concurrently, delithiated cathodes collapse, releasing oxygen that reacts violently with the electrolyte [16–18].

In terms of failure manifestations, overheating TR often involves jet flames and explosions. For instance, the 2023 Beijing residential battery explosion (three fatalities) released TR gases dominated by CO (18%) and H<sub>2</sub> (32%), igniting surrounding combustibles. Overcharging TR, however, typically manifests as smoldering, as seen in the 2024 Nanjing e-bike fire, where prolonged electrolyte decomposition sustained flame propagation.

Current research on TR mechanisms has advanced [6,8,19]. At the Institute of Energy Storage, Qingdao Energy Research Institute, *in situ* analysis revealed that H<sup>+</sup> ions at the anode of NCM cathode batteries exhibit poor thermal compatibility with electrolytes, acting as a primary trigger for chain reactions [20]. Experimental methods like adiabatic accelerating rate calorimetry (ARC) and differential scanning calorimetry (DSC) are widely used to determine TR critical temperatures but lack the capacity to analyze multi-factor coupled TR behaviors [21]. The state of charge (SOC) significantly impacts TR severity: high-SOC batteries exhibit more violent reactions due to higher active lithium content [22–24]. For example, Zeng et al. observed complete collapse of LiCoO<sub>2</sub> cathodes at critical overcharge states ( $x = 0.16$ ), releasing substantial heat [25]. For overheating TR mitigation, strategies include developing high-temperature-resistant separators (e.g., Al<sub>2</sub>O<sub>3</sub> coatings increasing TR onset temperature to 180 °C at 5  $\mu\text{m}$  thickness) and optimizing thermal management (liquid cooling systems reducing temperature rise rates by 60%) [26–29]. For overcharging TR, BMS voltage thresholds (<4.3 V) and electrolyte additives (e.g., LiBOB for aluminum current collector corrosion inhibition) are mainstream solutions [30–32]. However, existing studies focus on single-condition TR mechanisms, lacking systematic analysis of differences between overheating and overcharging TR or multi-scale suppression strategies.

This study investigates multi-mode TR triggers in 18650 ternary lithium-ion batteries (Li(NiCoMn)O<sub>2</sub> cathode), including overheating TR (external heating) and overcharging TR (voltage triggering). The goal is to elucidate temperature/pressure evolution, gas generation characteristics, jet flame behavior, and the influence of trigger mechanisms on TR dynamics.

## 2. Materials and Methods

### 2.1. Experimental Materials and Sample Preparation

The battery adopts a commercial 18650 lithium-ion cell (nominal capacity: 2.5 Ah, voltage: 3.6 V). The cathode material is LiNi<sub>0.6</sub>Co<sub>0.2</sub>Mn<sub>0.2</sub>O<sub>2</sub> (NCM622), the anode is graphite, and the electrolyte is 1 M LiPF<sub>6</sub>. The separator is a PE-based ceramic-coated membrane (thickness: 20  $\mu\text{m}$ , porosity: 45%). Its characteristics are as follows: dimensions: 18.2 mm (D) × 65.0 mm (H); charging cutoff voltage: 4.2 ± 0.05 V; nominal voltage: 3.7 V; rated capacity: 2450 mAh; storage temperature range: –20 °C to 40 °C; and cell weight: 44 ± 0.5 g.

### 2.2. Experimental Procedures

The schematic diagram of the experimental procedures is shown in Figure 1a. The battery was placed in a 25 °C constant-temperature chamber and left undisturbed for 24 h to ensure uniform state of charge (SOC) distribution. A high-precision Type K thermocouple array (accuracy ± 0.5 °C) was deployed to monitor temperatures at the cathode, anode, and sidewall center. The battery was secured in a thermal runaway test chamber, with

ceramic-coated heating plates (power density:  $0.5 \text{ W/cm}^2$ , coverage  $\geq 90\%$ ) clamped on both sides. The assembly was heated at  $5 \text{ }^\circ\text{C}/\text{min}$  until it reached the target temperature. When the thermocouples detected the onset temperature ( $T_0$ ) of self-heating reactions, external heating was halted, and a multichannel data acquisition system (sampling rate: 10 Hz) was activated to continuously record temperature, pressure, and visual dynamics. For overcharge tests, the battery was charged via a programmable charger (Neware BTS-4000, Neware Technology Limited, Dongguan, China) with a constant current of  $0.5 \text{ C}$ – $4.2 \text{ V}$ , followed by constant-voltage charging (positive electrode vent valve deactivated). Temperature evolution at the cathode, mid-layer, and anode (burst core distance: 0.15 m) was monitored in real time, while pressure data and released gases were collected.

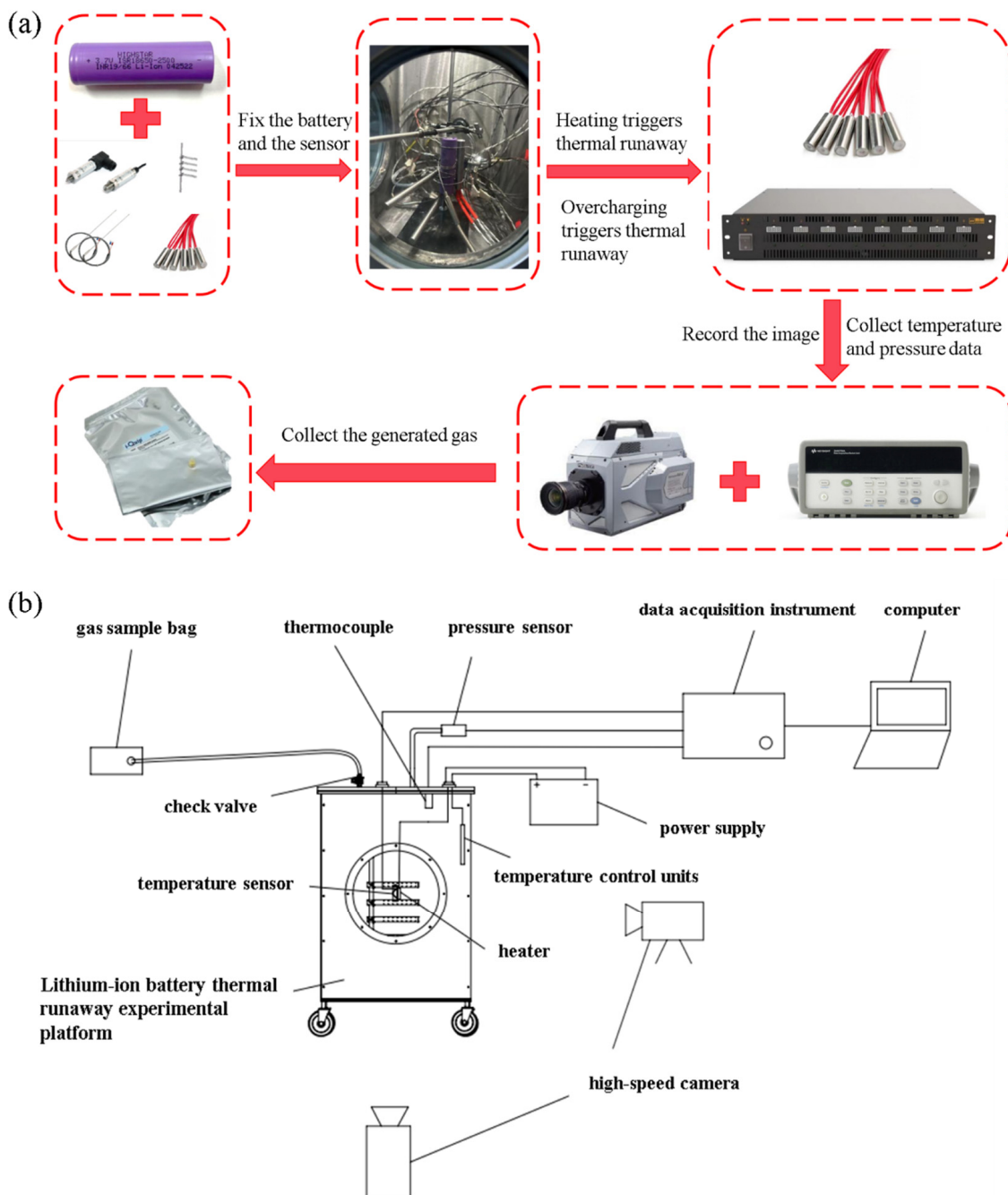


**Figure 1.** (a) Schematic diagram of the experimental procedures; (b) experimental platform for thermal runaway of lithium-ion batteries.

### 2.3. Experimental Platform

The experimental platform employs an in-house developed 18650 lithium-ion battery thermal runaway test system, as shown in Figure 1b. Thermodynamic data were collected using temperature sensors and a K-type thermocouple array. Pressure data were acquired via pressure sensors. Electrochemical parameters of the battery, including voltage precision ( $\pm 0.1$  mV), were recorded using a battery tester (Neware BTS-4000, Neware Technology Limited, Dongguan, China). Gas evolution characteristics during thermal runaway were analyzed using a gas chromatography–mass spectrometry (GC-MS) system (Agilent 7890B-5977A, Agilent Technologies, Palo Alto, CA, USA). Flame characteristics during thermal runaway were captured using a high-speed camera (Phantom V2512, Phantom V2512, Vision Research, Wayne, NJ, USA, resolution:  $1280 \times 800$ , frame rate: 10,000 fps).

## 3. Results

### 3.1. Temperature Characteristics of Lithium-Ion Batteries Under Different Thermal Runaway Conditions

The video images recorded through the observation window under overheating-induced thermal runaway conditions are shown in Figure 2. Initially, no significant changes were observed in the battery during heating. As the temperature rose, internal thermal runaway reactions began. At 195 s, white smoke started emitting from the battery, followed by jet flames erupting from the cathode. Approximately 5 s later, the battery exploded, with the cathode rupturing and the cell ejecting. Post-test battery images are shown in Figure 2e,f. Under overheating conditions, the temperature evolution at the cathode, mid-layer, and anode (Figure 3a) revealed distinct phases: From 0–100 s, minimal temperature variation at the cathode indicated slow Joule heat accumulation from external heat sources or localized internal short circuits, with temperatures remaining below the separator pore-closing threshold ( $\sim 80$  °C). During this period, only minor SEI (solid electrolyte interphase) film decomposition occurred, generating limited heat. Once the local temperature exceeded 80 °C, PE/PP-based separators underwent pore closure, blocking lithium-ion transport and sharply increasing internal resistance. This accelerated Joule heat generation, driving a gradual cathode temperature rise from 100 to 150 s [8,33]. Between 150 and 195 s, the cathode temperature surged from 80 °C to 516 °C due to chain exothermic reactions (e.g., electrolyte decomposition:  $\text{LiPF}_6 \rightarrow \text{LiF} + \text{PF}_5\uparrow$ ;  $\text{EC} \rightarrow \text{CO}\uparrow + \text{C}_2\text{H}_4\text{O}\uparrow$ ) at temperatures above 130 °C, which released flammable gases (CO, CH<sub>4</sub>, etc.) and approximately 500 J/g of heat. Concurrently, lattice oxygen release from NCM622 cathodes ( $>200$  °C) further intensified heat generation, causing a 436 °C temperature spike within 35 s [34].

The mid-layer temperature rose from ambient to 300 °C between 50 and 180 s, followed by a sharp increase to 460 °C at 185–195 s, before cooling to ambient temperature post-test. The anode temperature began rising at 100 s, reaching 50 °C at the bottom by 190 s. A rapid temperature surge to 425 °C (peak) occurred between 190 and 220 s, driven by internal short circuits and exothermic reactions, before gradual cooling to ambient temperature.

The peak temperatures and corresponding timestamps at the cathode, mid-layer, and anode of lithium-ion batteries under overheating-induced thermal runaway conditions are summarized in Table S1. The highest peak temperature was observed at the cathode (516 °C), primarily attributed to high-temperature oxygen evolution reactions and their self-catalytic nature. The cathode active material ( $\text{LiNiCoMnO}_2$ ) becomes structurally unstable above 200 °C, releasing lattice oxygen ( $\text{LiNiCoMnO}_2 \rightarrow \text{NiO} + \text{CoO} + \text{MnO} + \text{O}_2\uparrow$ ) accompanied by significant heat generation [35,36]. The released O<sub>2</sub> reacts violently with gases (e.g., CO and CH<sub>4</sub>) generated from electrolyte decomposition, further amplifying heat release. Due to the spatial position of the internal short-circuit point and the influence of the thermal diffusion path, the mid-layer reaches the peak (460 °C) first. Its peak temperature

is lower than that of the positive electrode but higher than that of the negative electrode. The mid-layer exhibited the earliest temperature rise (starting at 50 s), indicating that the internal short-circuit point proximity to the geometric center of the battery. During initial short-circuiting, Joule heat diffused radially via current collectors, prioritizing mid-layer heating. However, despite initiating the shortest path, the mid-layer's lower exothermic capacity compared to cathode active materials and faster heat dissipation to the outer casing resulted in a lower final peak temperature than the cathode. The anode exhibited the latest peak timing, and its peak temperature ( $425^{\circ}\text{C}$ ) is significantly lower than both the cathode and mid-layer. This is due to the delayed decomposition of the SEI film on graphite anodes ( $>250^{\circ}\text{C}$ ,  $\text{Li}_2\text{CO}_3 \rightarrow \text{Li}_2\text{O} + \text{CO}_2\uparrow$ ) with lower heat output [37]. Additionally, the high activation energy of graphite oxidation ( $\text{C} + \text{O}_2 \rightarrow \text{CO}_2\uparrow$ ) slows reaction kinetics compared to cathode oxygen release processes [38].

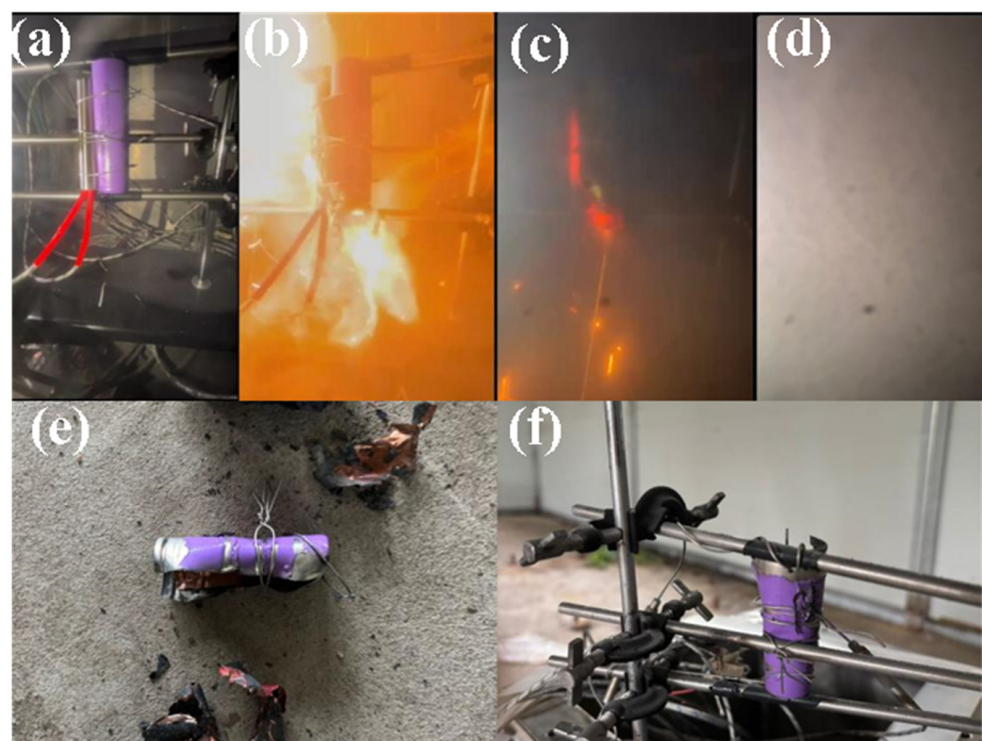


**Figure 2.** Photos of the experimental process of thermal runaway of lithium-ion batteries under overheating conditions: (a) initial state; (b) jet flame ejection; (c) the flame weakens; (d) generation of a large amount of smoke; (e,f) the battery after thermal runaway.

Under overcharging-induced thermal runaway conditions, the video images recorded through the observation window are shown in Figure 4. As the lithium-ion battery was continuously overcharged, slight swelling occurred in the mid-layer of the battery without any white smoke emission. Subsequently, jet flames erupted from the cathode, accompanied by massive white smoke release, followed by an immediate explosion.

The temperature evolution at the cathode, mid-layer, and anode under overcharging conditions is illustrated in Figure 3b. During overcharging, the cathode exhibited a slow linear temperature rise from 50 to 800 s, attributed to localized internal short circuits caused by lithium dendrite growth and SEI (solid electrolyte interphase) film decomposition. After 800 s, the cathode temperature sharply increased to a peak of  $411^{\circ}\text{C}$ , driven by the combined effects of large-scale internal short circuits induced by lithium dendrites and structural collapse of the cathode material [39]. The cathode temperature rise rate was significantly higher than those of the mid-layer and anode, indicating that cathode oxidation reactions dominated the runaway process. When the voltage exceeded 4.5 V, electrolyte

oxidation decomposition occurred on the cathode surface (reaction:  $\text{EC} \rightarrow \text{CO}_3^{2-} + \text{C}_2\text{H}_4 \uparrow$ ), releasing  $\text{CO}_2$  and  $\text{O}_2$ , which further accelerated thermal runaway.

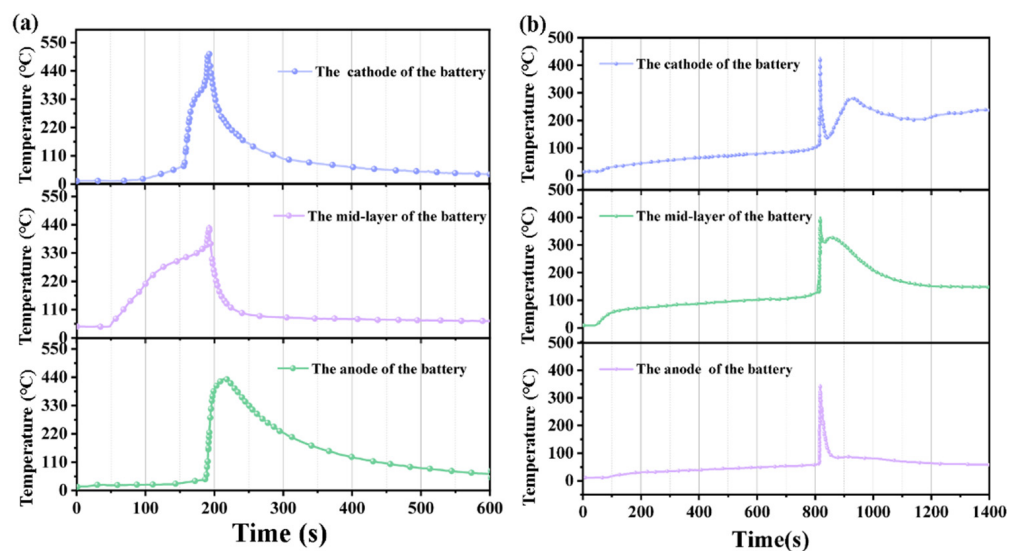


**Figure 3.** (a) The temperature variation curves of the cathode, mid-layer, and anode of lithium-ion batteries during thermal runaway under overheating conditions; (b) The temperature variation curves of the cathode, mid-layer, and anode of lithium-ion batteries during thermal runaway under overheating conditions.



**Figure 4.** Photos of the experimental process of thermal runaway of lithium-ion batteries under overcharging conditions: (a) initial state; (b) jet flame ejection; (c) generation of a large amount of smoke; (d) the battery after thermal runaway.

Notably, the cathode temperature remained higher than the mid-layer ( $400^\circ\text{C}$ ) and anode throughout the process. The  $11^\circ\text{C}$  temperature difference between the cathode ( $411^\circ\text{C}$ ) and mid-layer ( $400^\circ\text{C}$ ) is attributed to uneven current density distribution caused by tortuous conductive paths formed by lithium dendrites penetrating the separator, leading to delayed mid-layer heating. A secondary temperature peak in the cathode between 800 and 900 s may arise from the disproportionation reaction of residual  $\text{NiO}$  and secondary reactions of  $\text{LiPF}_6$  decomposition products.

The peak temperatures and corresponding timestamps at the cathode, mid-layer, and anode under overcharging conditions are summarized in Table S2. The cathode exhibited the highest peak temperature, followed by the mid-layer and anode. This aligns with the flame propagation pattern (jet flames primarily along the cathode direction) observed under overcharging conditions, consistent with the temperature and flame dynamics during overheating-induced thermal runaway. However, the temperatures under overcharging were slightly lower than those under overheating conditions. This discrepancy may stem

from differences in thermal measurement methods: thermocouple readings during overcharging reflect ambient temperatures, whereas overheating experiments involved localized heating rods ( $>700\text{ }^{\circ}\text{C}$ ), potentially elevating surface temperatures beyond actual battery surface values.

### 3.2. Pressure Characteristics of Lithium-Ion Batteries Under Different Thermal Runaway Conditions

The pressure evolution profiles at the cathode, mid-layer, and anode under overheating-induced thermal runaway conditions are shown in Figure 5a. All three regions exhibited instantaneous large-pressure spikes, with the cathode showing the highest peak pressure (0.537 MPa), followed by the mid-layer (0.392 MPa) and anode (0.310 MPa). This gradient arises because the cathode's layered structure collapses during thermal runaway, releasing lattice oxygen ( $\text{LiNiCoMnO}_2 \rightarrow \text{NiO} + \text{CoO} + \text{MnO} + \text{O}_2\uparrow$ ) that reacts violently with electrolytes (e.g., EC  $\rightarrow \text{CO}_2\uparrow + \text{H}_2\text{O}$  vapor), generating high gas volumes ( $\text{CO}_2$ ,  $\text{H}_2\text{O}$ , etc.). Meanwhile, gas accumulation in the mid-layer is constrained by the separator, leading to slower volume expansion compared to the cathode, resulting in a slightly lower peak pressure. The anode's minimal pressure increase (0.310 MPa) stems from slow SEI (solid electrolyte interphase) film decomposition (e.g.,  $\text{Li}_2\text{CO}_3 \rightarrow \text{Li}_2\text{O} + \text{CO}_2\uparrow$ ), which produces gases at a slower rate.

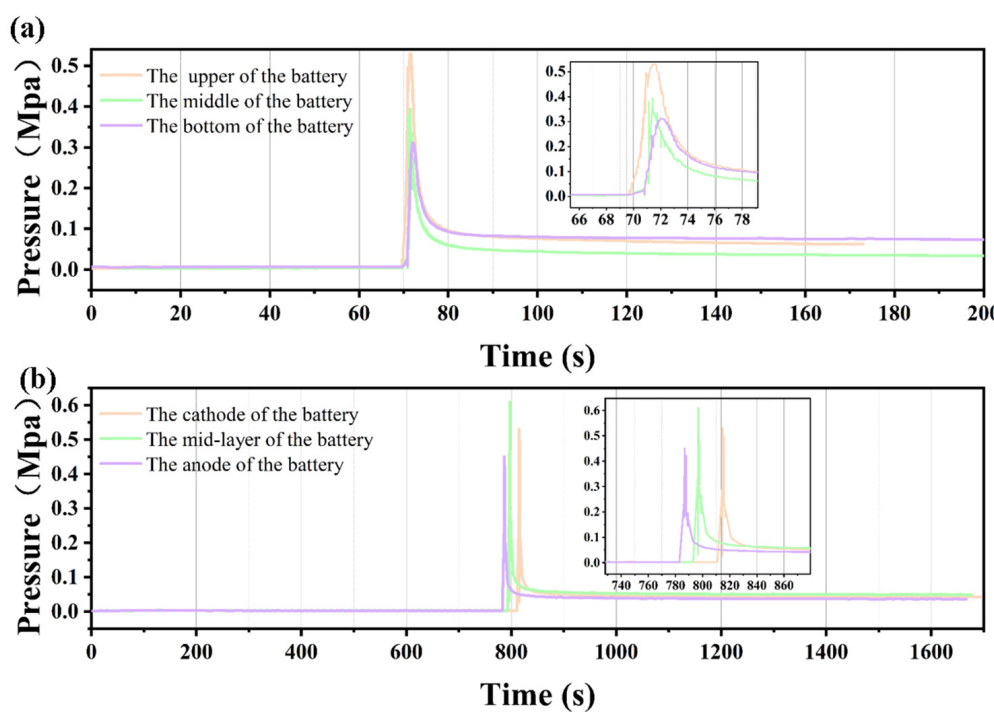


**Figure 5.** (a) The pressure variation curves of the cathode, mid-layer, and anode of lithium-ion batteries during thermal runaway under overheating conditions; (b) the pressure variation curves of the cathode, mid-layer, and anode of lithium-ion batteries during thermal runaway under overcharging conditions.

Under overcharging-induced thermal runaway (Figure 5b), the pressure peaks were 0.531 MPa (cathode), 0.601 MPa (mid-layer), and 0.452 MPa (anode). The mid-layer's higher pressure reflects intense electrolyte decomposition (e.g.,  $\text{LiPF}_6 \rightarrow \text{LiF} + \text{PF}_5\uparrow$ ) combined with restricted gas diffusion, while the cathode's slightly lower peak is due to rapid oxygen release constrained by structural integrity. The anode's minimal pressure increase is attributed to slow gas generation (e.g.,  $\text{C} + \text{O}_2 \rightarrow \text{CO}_2\uparrow$ ) and efficient venting paths. During the overcharging thermal runaway process of lithium-ion batteries, there are significant

differences in the time at which the pressure peaks in the cathode, mid-layer, and anode reach their peak values. This temporal characteristic is closely related to the reaction kinetics and mass transfer processes in different regions. The earliest peak of the anode electrode is due to the SEI film decomposition and lithium solvent reaction triggered by lithium deposition on the negative electrode, which are activated in the early stage of overcharging. The delay in peak pressure in the mid-layer is due to the combined effect of electrolyte decomposition (such as EC  $\rightarrow$  CO<sub>2</sub>) and gas diffusion obstruction, resulting in a rapid increase in pressure during the overcharge phase. The pressure peak in the cathode region appeared latest, primarily due to the structural collapse of the positive electrode material (such as NCM layered decomposition) and the need for higher temperatures ( $>700$  °C) for oxygen release. Therefore, its pressure peak usually appears in the later stage of thermal runaway. This temporal difference reflects the dynamic competitive relationship between material degradation mechanisms (such as SEI rupture and positive electrode phase transition) and thermal electrochemical coupling processes.

### 3.3. Gas Production Characteristics of Lithium-Ion Batteries Under Different Thermal Runaway Conditions

The gas components generated by lithium-ion batteries after overheating and losing control include a large number of organic and flammable gases such as CH<sub>4</sub>, C<sub>2</sub>H<sub>6</sub>, C<sub>2</sub>H<sub>4</sub>, C<sub>3</sub>H<sub>8</sub>, C<sub>4</sub>H<sub>8</sub>, C<sub>5</sub>H<sub>12</sub>, CO<sub>2</sub>, CO, and H<sub>2</sub>. The normalized gas composition is shown in Figure 6a. Among them, CO<sub>2</sub> and H<sub>2</sub> have the highest proportions, accounting for 54.7% and 29.7%, respectively. CO<sub>2</sub> may originate from the thermal decomposition of SEI film, lithium carbonate, electrolyte lithium salt LiPF<sub>6</sub>, and the combustion of electrolyte. H<sub>2</sub> may originate from electrode adhesives such as polyvinylidene fluoride (PVDF) and sodium carboxymethyl cellulose (CMC) reacting with Li. CO accounts for 7.5%, being mainly from the reaction between Li embedded on the negative electrode and CO<sub>2</sub>, as well as the reaction between Li embedded on the negative electrode and electrolyte [40]. The total proportion of hydrocarbon gases such as methane and ethylene is less than 10%, being mainly derived from the reaction between electrolyte solvents and Li. The main components of the gas generated by overcharging runaway in lithium-ion batteries are similar to those under overheating runaway conditions, still dominated by CO<sub>2</sub>, H<sub>2</sub>, CO, and olefin gases. The normalized gas composition is shown in Figure 6b. However, it can be observed that compared to the condition of overheating out of control, the proportion of hydrogen gas decreases under overcharge out-of-control conditions, indicating that overcharge conditions inhibit hydrogen evolution reactions. Under overcharge conditions, the high voltage preferentially triggers electrolyte oxidation rather than lithium deposition. At this time, H<sub>2</sub> mainly comes from the secondary reaction after the release of positive electrode oxygen, and the rate of H<sub>2</sub> production decreases. On the other hand, under overcharge conditions, the proportion of CO<sub>2</sub> increases, indicating that a high voltage accelerates the decomposition of positive electrode materials. Overall, the gas produced by overheating and loss of control is mainly CO<sub>2</sub> and H<sub>2</sub>, reflecting the dominant decomposition of positive electrode materials; the proportion of H<sub>2</sub> decreases due to overcharging and thermal runaway, but the proportion of CO and hydrocarbon gases increases, indicating an intensification of electrolyte oxidation and electrochemical reactions. There are essential differences between the two in terms of thermal runaway pathways, gas toxicity, and safety risks, and targeted thermal management and monitoring strategies need to be designed.

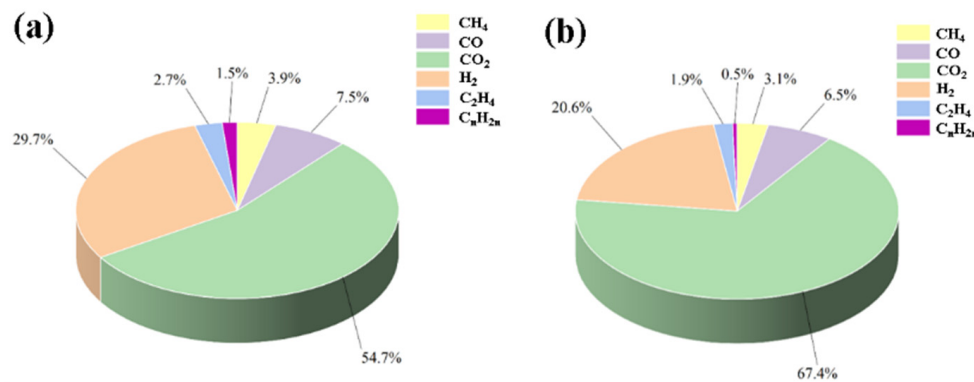


**Figure 6.** (a) The main types and volume fractions of gases released during thermal runaway of lithium-ion batteries under overheating conditions; (b) the main types and volume fractions of gases released during thermal runaway of lithium-ion batteries under overcharging conditions.

## 4. Discussion

### 4.1. Heat Release During the Thermal Runaway Process

The heat accumulation rate of the battery before thermal runaway can be calculated using Equation (1).

$$P_b = c_b m_b \frac{dT}{dt} \quad (1)$$

In the formula,  $c_b = 1.0 \text{ kJ}/(\text{kg}\cdot^\circ\text{C})$  represents the heat capacity of the battery;  $m_b$  represents the mass of the battery after the test; and  $\frac{dT}{dt}$  is the first-order derivative of temperature varying with time.

As can be seen in Figure 3b, when thermal runaway occurs under overheating conditions, the temperature distribution in the cathode, mid-layer, and anode of the lithium battery is uneven, and the changes are also different. Generally, they can all be divided into two stages, as shown in Table S3. The average heat accumulation power can be calculated using the average value of each stage. After the test, the mass of the battery was measured ( $m_b = 38.7 \text{ g}$ ), and the average heat accumulation rate was calculated to be 24.3 W.

$$\overline{P}_{bh} = \frac{c_b m_b \frac{dT_1}{dt_1} + c_b m_b \frac{dT_2}{dt_2} + c_b m_b \frac{dT_3}{dt_3} + c_b m_b \frac{dT_4}{dt_4} + c_b m_b \frac{dT_5}{dt_5} + c_b m_b \frac{dT_6}{dt_6}}{6} = 24.3 \text{ W}$$

As can be seen in Figure 3b, when thermal runaway occurs under overcharging conditions, the temperature distribution of the battery is uneven. Therefore, the average temperature change rates of the positive electrode, negative electrode, and the middle region are used for calculation. The rates of temperature changes of the cathode, mid-layer, and anode are shown in Table S4. After the test, the mass of the battery is 37.9 g, and the average heat accumulation rate calculation is 4W. The average heat accumulation rate under overheating conditions is much higher than that under overcharging conditions. This is because the heat lost control due to overheating mainly comes from the direct input of the external heating device, while the heat lost control due to overcharging is only the internal electrochemical reaction and ohmic heat, which accumulates with the charging time and takes a relatively long time to reach the critical temperature.

The total heat release can be calculated using Equation (2).

$$H_t = c_b m_b (T_t - T_0) \quad (2)$$

In the formula,  $H_t$  represents the total heat release of the battery;  $c_b$  represents the heat capacity of the battery;  $m_b$  represents the quality of the battery after testing;  $T_t$  represents the peak temperature; and  $T_0$  represents the ambient temperature.

As can be seen in Figure 3, the heat distribution of lithium batteries during thermal runaway is uneven. Further considering the mass distribution of the cathode, mid-layer, and anode of the battery, when calculating the total heat, the mass fractions of the cathode, mid-layer, and anode (25%, 50%, and 25%) can be multiplied by the heat released.

Firstly, the temperature variation under overheating conditions was analyzed. The initial test temperature was 10 °C, the peak temperature of the positive electrode was 516 °C, the peak temperature of the middle region was 460 °C, and the peak temperature of the negative electrode region was 425 °C. Therefore, the  $\Delta T$  ( $T_t - T_0$ ) of the cathode is 506 K, the  $\Delta T$  of the mid-layer is 450 K, and the  $\Delta T$  of the anode is 415 K.

Based on this calculation, it can be known that the total heat release of thermal runaway of lithium-ion batteries under overheating conditions is 17.6 KJ. However, since the temperature sensor collects the field temperature, during the process of overheating and runaway, which is affected by the high temperature of the heating rod, the temperature data collected by the sensor may be higher than the surface temperature of the lithium-ion battery. Therefore, the total heat release during the thermal runaway of the lithium-ion battery will be slightly lower than 17.6 KJ. The total heat release from thermal runaway of lithium-ion batteries under overcharge runaway conditions is estimated to be approximately 14.2 KJ by a similar method. It should also be noted that these data are an approximate estimation of the heat release during the thermal runaway process of lithium-ion batteries based on temperature data and under ideal adiabatic conditions.

During the thermal runaway process of lithium-ion batteries, the internal energy of the battery decreases and is converted into thermal energy for release. Under near-adiabatic conditions, all the heat released leads to an increase in temperature. Therefore, the change in internal energy during the thermal runaway process of lithium-ion batteries can be inferred through the variation of temperature.

The relationship between internal energy and temperature can be expressed as Equation (3).

$$Q = c_b m_b \Delta T \quad (3)$$

Thermal runaway under overheating conditions mainly has two stages. In the first stage, when the temperature is less than 80 °C, only a slight decomposition of the SEI film occurs, with a relatively low heat generation and an internal energy of 3.15 KJ. In the second stage, the battery undergoes a chain exothermic reaction, with the temperature sharply rising to 516 °C, releasing a large amount of heat. At this point, the internal energy is 19.6 KJ.

Under overcharging conditions, the initial temperature rose slowly and linearly to 100 °C. This was due to the local internal short circuit caused by the growth of lithium dendrites and the decomposition of the SEI film. The internal energy was calculated to be 3.4 KJ. After 800 s, the temperature rose sharply to the peak of 411 °C, and the internal energy was calculated to be 15.2 KJ. This heat is derived from the coupling effect of large-area internal short circuits caused by lithium dendrites and the structural collapse of the cathode material.

#### 4.2. Security Protection Strategy

Figure S1 shows the charge–discharge curves of the lithium battery at a rate of 0.5 C: in (a), the cut-off voltage is 4.2 V, and in (b), the cut-off voltage is 4.6V. Figure S1b shows that the voltage curve becomes steep and the platform disappears after the battery voltage exceeds 4.2 V, indicating that polarization intensifies at this time. After the battery is

overcharged to 4.5 V, the voltage drops sharply, indicating that the electrolyte undergoes oxidation and decomposition, generating a large amount of gas and causing a sudden increase in the internal pressure of the battery. The accumulation of gas causes the electrode spacing to increase, the internal resistance rises sharply, and the current is forced to be interrupted. Compared with the normal charge and discharge capacity of 2230 mAh, the capacity of lithium-ion batteries decreases to 1762 mAh after overcharging, which is closely related to the damage of the SEI film and the lithium plating phenomenon caused by overcharging. The internal resistance of the lithium battery after overcharge was measured by the four-wire method of the resistance meter to be 21 mΩ. Compared with the internal resistance of 6 mΩ of the battery at normal charge and discharge, it has increased significantly, indicating that overcharging has led to the damage of the electrode structure.

Overheating-driven gas profiles reflect cathode material decomposition (e.g., NCM622 → NiO + CoO + MnO + O<sub>2</sub>↑) and self-catalytic electrolyte combustion (LiPF<sub>6</sub> → LiF + PF<sub>5</sub>↑; EC → CO↑ + C<sub>2</sub>H<sub>4</sub>O↑), producing rapid O<sub>2</sub> release and high-pressure peaks at the cathode (0.537 MPa). In contrast, overcharging triggers lithium dendrite-induced internal short circuits (post-800 s), combining cathode collapse and electrolyte oxidation (EC → CO<sub>3</sub><sup>2-</sup> + C<sub>2</sub>H<sub>4</sub>↑) to generate faster gas release with mid-layer pressure spikes (0.601 MPa) due to restricted gas diffusion. The distinct gas compositions—CO<sub>2</sub>/H<sub>2</sub> dominance in overheating versus elevated CO<sub>2</sub> and suppressed H<sub>2</sub> in overcharging—highlight divergent failure mechanisms: cathode-driven thermal runaway versus electrolyte oxidation and electrochemical intensification under high voltage.

Therefore, safety strategies must prioritize material-specific and system-level controls. For overheating mitigation, Al<sup>3+</sup> doping or Al<sub>2</sub>O<sub>3</sub> coating suppresses cathode oxygen release, while PTC materials integrated into electrodes enable current self-limiting during thermal runaway. Graded pressure valves (0.4 MPa threshold) combined with N<sub>2</sub> inerting mitigate re-ignition risks. For overcharging protection, BMS redundancy (primary 4.2 V + redundant 4.3 V thresholds) triggers charging termination and balancing circuits, supplemented by FEC (fluoroethylene carbonate) additives to stabilize SEI and TPP (triphenyl phosphate) to suppress electrolyte oxidation. High-temperature ceramic-coated PP separators delay gas diffusion and reduce mid-layer pressure peaks.

These findings underscore the necessity for tailored thermal management and multi-layered safety protocols addressing the unique gas dynamics, reaction pathways, and failure modes of overheating versus overcharging scenarios in high-energy-density lithium-ion batteries.

## 5. Conclusions

This study systematically contrasts the thermal runaway behaviors and safety risks of lithium-ion batteries under overheating-induced and overcharging-induced thermal runaway conditions. Through a customized experimental platform, the dynamic evolution mechanisms and safety protection requirements of thermal runaway in both abuse scenarios were revealed. Based on key experimental differences, differentiated safety strategies were proposed, providing theoretical and technical pathways for designing and protecting high-safety lithium-ion batteries. In overheating-induced thermal runaway, the cathode material releases lattice oxygen above 200 °C (NCM622 → NiO + CoO + MnO + O<sub>2</sub>↑), initiating a self-catalytic chain reaction with electrolyte decomposition (LiPF<sub>6</sub> → LiF + PF<sub>5</sub>↑; EC → CO↑ + C<sub>2</sub>H<sub>4</sub>O↑), causing the cathode temperature to surge from 80 °C to 516 °C within 195 s, forming the core heat generation zone with an instantaneous pressure peak of 0.537 MPa. Gas composition is dominated by CO<sub>2</sub> (54.7%) and H<sub>2</sub> (29.7%). Mitigation strategies include Al<sup>3+</sup> doping to suppress lattice oxygen release and integrating PTC materials for current self-limiting to block thermal propagation. In overcharging-induced thermal runaway, lithium

dendrites piercing the separator after 800 s trigger internal short circuits combined with cathode structural collapse and electrolyte oxidation ( $\text{EC} \rightarrow \text{CO}_3^{2-} + \text{C}_2\text{H}_4 \uparrow$ ), resulting in a lower cathode peak temperature (411 °C) but faster gas generation. Restricted gas diffusion in the mid-layer creates a pressure peak of 0.601 MPa, with  $\text{CO}_2$  dominating (67.4%) and  $\text{H}_2$  reduced to 20.6%, indicating intensified electrolyte oxidation. Protective measures involve optimizing BMS thresholds (4.2 V primary + 4.3 V redundant) and incorporating FEC/TPP additives to stabilize SEI and suppress gas evolution. Comparative analysis highlights distinct thermal runaway pathways: overheating is driven by cathode oxygen release and self-catalytic electrolyte combustion, while overcharging involves electrolyte oxidation and dendrite-induced short circuits. Safety strategies must therefore prioritize material-specific modifications (e.g.,  $\text{Al}^{3+}$  doping and SEI-stabilizing additives) and system-level controls (e.g., redundant BMS thresholds and high-temperature separators) to address the unique risks of each abuse scenario, ensuring comprehensive protection against complex thermal runaway triggers in high-energy-density batteries.

**Supplementary Materials:** The following supporting information can be downloaded at: <https://www.mdpi.com/article/10.3390/batteries11070242/s1>. Figure S1: (a) The charge–discharge curve of lithium-ion batteries at a rate of 0.5C; (b) the charge–discharge curve of lithium-ion batteries under overcharge conditions at a rate of 0.5C; Table S1. Peak temperatures and times of the cathode, mid-layer, and anode of lithium-ion batteries under overheating conditions; Table S2. Peak temperatures and times of the cathode, mid-layer, and anode of lithium-ion batteries under overcharging conditions; Table S3: The rate of temperature change of lithium batteries before thermal runaway under overheating conditions; Table S4: The rate of temperature change of lithium batteries before thermal runaway under overcharging conditions; Figure S2: Comparison of the representative gas ( $\text{CO}_2$ ,  $\text{H}_2$ , and CO) production volumes generated by thermal runaway of lithium batteries under overheating and overcharging conditions.

**Author Contributions:** Conceptualization, Y.Y.; Data curation, H.L.; Investigation, L.L., H.X., Y.C., Y.W. and Z.Z.; Methodology, Y.Y., J.G. and Z.Z.; Writing—original draft, Y.Y.; Writing—review and editing, Z.Z. Resources, Y.Q. and S.Y. All authors have read and agreed to the published version of the manuscript.

**Funding:** This work was supported by the State Key Laboratory of Disaster Prevention & Mitigation of Explosion & Impact (No. LGD-SKL-202203), the Nature Science Foundation of Jiangsu Province (No. BK20241602), and the Army Engineering University Youth Independent Innovation Fund (No. KYFYJKQTZQ23006).

**Data Availability Statement:** The data that support the findings of this study are available from the corresponding author upon reasonable request.

**Conflicts of Interest:** The authors declare no conflicts of interest.

## References

1. Kim, T.; Song, W.; Son, D.-Y.; Ono, L.K.; Qi, Y. Lithium-ion batteries: Outlook on present, future, and hybridized technologies. *J. Mater. Chem. A* **2019**, *7*, 2942–2964. [[CrossRef](#)]
2. Li, M.; Lu, J.; Chen, Z.; Amine, K. 30 years of lithium-ion batteries. *Adv. Mater.* **2018**, *30*, 1800935–1809648. [[CrossRef](#)] [[PubMed](#)]
3. Manthiram, A. An outlook on lithium ion battery technology. *ACS Cent. Sci.* **2017**, *3*, 1063–1069. [[CrossRef](#)]
4. Xie, J.; Lu, Y.-C. A retrospective on lithium-ion batteries. *Nat. Commun.* **2020**, *11*, 2499. [[CrossRef](#)] [[PubMed](#)]
5. Feng, X.; Ren, D.; He, X.; Ouyang, M. Mitigating thermal runaway of lithium-ion batteries. *Joule* **2020**, *4*, 743–770. [[CrossRef](#)]
6. Wang, Q.; Ping, P.; Zhao, X.; Chu, G.; Sun, J.; Chen, C. Thermal runaway caused fire and explosion of lithium ion battery. *J. Power Sources* **2012**, *208*, 210–224. [[CrossRef](#)]
7. Kong, D.; Lv, H.; Ping, P.; Wang, G. A review of early warning methods of thermal runaway of lithium ion batteries. *J. Energy Storage* **2023**, *64*, 107073. [[CrossRef](#)]
8. Feng, X.; Ouyang, M.; Liu, X.; Lu, L.; Xia, Y.; He, X. Thermal runaway mechanism of lithium ion battery for electric vehicles: A review. *Energy Storage Mater.* **2018**, *10*, 246–267. [[CrossRef](#)]

9. Mallick, S.; Gayen, D. Thermal behaviour and thermal runaway propagation in lithium-ion battery systems—A critical review. *J. Energy Storage* **2023**, *62*, 106894. [[CrossRef](#)]
10. Hu, X.; Gao, F.; Xiao, Y.; Wang, D.; Gao, Z.; Huang, Z.; Ren, S.; Jiang, N.; Wu, S. Advancements in the safety of Lithium-Ion Battery: The Trigger, consequence and mitigation method of thermal runaway. *Chem. Eng. J.* **2024**, *481*, 148450. [[CrossRef](#)]
11. Kong, L.; Li, Y.; Feng, W. Strategies to solve lithium battery thermal runaway: From mechanism to modification. *Electrochem. Energy Rev.* **2021**, *4*, 633–679. [[CrossRef](#)]
12. Galushkin, N.E.; Yazvinskaya, N.N.; Galushkin, D.N. Causes and mechanism of thermal runaway in lithium-ion batteries, contradictions in the generally accepted mechanism. *J. Energy Storage* **2024**, *86*, 111372. [[CrossRef](#)]
13. Yang, Y.; Wang, R.; Shen, Z.; Yu, Q.; Xiong, R.; Shen, W. Towards a safer lithium-ion batteries: A critical review on cause, characteristics, warning and disposal strategy for thermal runaway. *Adv. Appl. Energy* **2023**, *11*, 100146. [[CrossRef](#)]
14. He, D.; Wang, J.; Peng, Y.; Li, B.; Feng, C.; Shen, L.; Ma, S. Research advances on thermal runaway mechanism of lithium-ion batteries and safety improvement. *Sustain. Mater. Technol.* **2024**, *41*, e01017. [[CrossRef](#)]
15. Feng, X.; Zheng, S.; Ren, D.; He, X.; Wang, L.; Cui, H.; Liu, X.; Jin, C.; Zhang, F.; Xu, C. Investigating the thermal runaway mechanisms of lithium-ion batteries based on thermal analysis database. *Appl. Energy* **2019**, *246*, 53–64. [[CrossRef](#)]
16. Yan, W.; Huang, W.; Yang, Y.; Wei, Z.; Zhen, H.; Lin, Y. Research on overcharge mitigations and thermal runaway risk of 18650 lithium-ion batteries. *J. Energy Storage* **2025**, *120*, 116372. [[CrossRef](#)]
17. Liu, Z.; Guo, X.; Meng, N.; Yu, Z.; Yang, H. Study of thermal runaway and the combustion behavior of lithium-ion batteries overcharged with high current rates. *Thermochim. Acta* **2022**, *715*, 179276. [[CrossRef](#)]
18. Zhou, G.; Lu, H.; Zhang, Q.; Yang, S.; Liu, Y.; Niu, C.; Kong, Y.; Huang, Q.; Wei, Z. Experimental study on thermal runaway and flame eruption characteristics of NCM523 lithium-ion battery induced by the coupling stimulations of overcharge-penetration. *Process Saf. Environ. Prot.* **2024**, *191*, 131–145. [[CrossRef](#)]
19. Li, Y.; Liu, X.; Wang, L.; Feng, X.; Ren, D.; Wu, Y.; Xu, G.; Lu, L.; Hou, J.; Zhang, W. Thermal runaway mechanism of lithium-ion battery with  $\text{LiNi}_{0.8}\text{Mn}_{0.1}\text{Co}_{0.1}\text{O}_2$  cathode materials. *Nano Energy* **2021**, *85*, 105878. [[CrossRef](#)]
20. Huang, L.; Xu, G.; Du, X.; Li, J.; Xie, B.; Liu, H.; Han, P.; Dong, S.; Cui, G.; Chen, L. Uncovering LiH triggered thermal runaway mechanism of a high-energy  $\text{LiNi}_{0.5}\text{Co}_{0.2}\text{Mn}_{0.3}\text{O}_2$ /graphite pouch cell. *Adv. Sci.* **2021**, *8*, 2100676. [[CrossRef](#)]
21. Yue, Y.; Jia, Z.; Li, Y.; Wen, Y.; Lei, Q.; Duan, Q.; Sun, J.; Wang, Q. Thermal runaway hazards comparison between sodium-ion and lithium-ion batteries using accelerating rate calorimetry. *Process Saf. Environ. Prot.* **2024**, *189*, 61–70. [[CrossRef](#)]
22. Qi, C.; Liu, Z.; Lin, C.; Liu, X.; Liu, D.; Li, Z.; Yi, A. The gas production characteristics and catastrophic hazards evaluation of thermal runaway for  $\text{LiNi}_{0.5}\text{Co}_{0.2}\text{Mn}_{0.3}\text{O}_2$  lithium-ion batteries under different SOCs. *J. Energy Storage* **2024**, *88*, 111678. [[CrossRef](#)]
23. Liao, Z.; Zhang, S.; Li, K.; Zhao, M.; Qiu, Z.; Han, D.; Zhang, G.; Habetsler, T.G. Hazard analysis of thermally abused lithium-ion batteries at different state of charges. *J. Energy Storage* **2020**, *27*, 101065. [[CrossRef](#)]
24. Zhang, Q.; Niu, J.; Zhao, Z.; Wang, Q. Research on the effect of thermal runaway gas components and explosion limits of lithium-ion batteries under different charge states. *J. Energy Storage* **2022**, *45*, 103759. [[CrossRef](#)]
25. Zeng, Y.; Wu, K.; Wang, D.; Wang, Z.; Chen, L. Overcharge investigation of lithium-ion polymer batteries. *J. Power Sources* **2006**, *160*, 1302–1307. [[CrossRef](#)]
26. Song, Y.; Liu, X.; Ren, D.; Liang, H.; Wang, L.; Hu, Q.; Cui, H.; Xu, H.; Wang, J.; Zhao, C. Simultaneously blocking chemical crosstalk and internal short circuit via gel-stretching derived nanoporous non-shrinkage separator for safe lithium-ion batteries. *Adv. Mater.* **2022**, *34*, 2106335. [[CrossRef](#)]
27. Liu, H.; Liu, C.; Zhou, Y.; Zhang, Y.; Deng, W.; Zou, G.; Hou, H.; Ji, X. The application of  $\text{Al}_2\text{O}_3$  in separators and solid electrolytes of lithium-ion battery: A review. *Energy Storage Mater.* **2024**, *71*, 103575. [[CrossRef](#)]
28. Shang, Z.; Qi, H.; Liu, X.; Ouyang, C.; Wang, Y. Structural optimization of lithium-ion battery for improving thermal performance based on a liquid cooling system. *Int. J. Heat Mass Transf.* **2019**, *130*, 33–41. [[CrossRef](#)]
29. Akbarzadeh, M.; Kalogiannis, T.; Jaguemont, J.; Jin, L.; Behi, H.; Karimi, D.; Beheshti, H.; Van Mierlo, J.; Berecibar, M. A comparative study between air cooling and liquid cooling thermal management systems for a high-energy lithium-ion battery module. *Appl. Therm. Eng.* **2021**, *198*, 117503. [[CrossRef](#)]
30. Gabbar, H.A.; Othman, A.M.; Abdussami, M.R. Review of battery management systems (BMS) development and industrial standards. *Technologies* **2021**, *9*, 28. [[CrossRef](#)]
31. Li, J.; Yang, J.; Ji, Z.; Su, M.; Li, H.; Wu, Y.; Su, X.; Zhang, Z. Prospective Application, Mechanism, and Deficiency of Lithium Bis (oxalate) Borate as the Electrolyte Additive for Lithium-Batteries. *Adv. Energy Mater.* **2023**, *13*, 2301422. [[CrossRef](#)]
32. Haregewoin, A.M.; Wotango, A.S.; Hwang, B.-J. Electrolyte additives for lithium ion battery electrodes: Progress and perspectives. *Energy Environ. Sci.* **2016**, *9*, 1955–1988. [[CrossRef](#)]
33. Peng, S.; Li, K.; Liu, P.; Zhang, W.; Wu, W.; Han, X.; Cao, Y.-c.; Wen, J.; Cheng, S. Dynamics of multidimensional signals in lithium-ion battery during thermal runaway under various oven temperatures. *J. Energy Storage* **2025**, *108*, 115071. [[CrossRef](#)]

34. Song, Y.; Cui, Y.; Li, B.; Geng, L.; Yan, J.; Zhu, D.; Zhou, P.; Zhou, J.; Yan, Z.; Xue, Q. Revealing the origin of high-thermal-stability of single-crystal Ni-rich cathodes toward higher-safety batteries. *Nano Energy* **2023**, *116*, 108846. [[CrossRef](#)]
35. Jia, Y.; Hou, X.; Li, K.; Wang, L.; Zhang, M.; Li, Z.; Xu, X.; Zheng, J. Unraveling the oxygen evolution in layered  $\text{LiNiO}_2$  with the role of Li/Ni disordering. *Energy Storage Mater.* **2024**, *71*, 103632. [[CrossRef](#)]
36. House, R.A.; Marie, J.-J.; Pérez-Osorio, M.A.; Rees, G.J.; Boivin, E.; Bruce, P.G. The role of  $\text{O}_2$  in O-redox cathodes for Li-ion batteries. *Nat. Energy* **2021**, *6*, 781–789. [[CrossRef](#)]
37. Liu, X.; Yin, L.; Ren, D.; Wang, L.; Ren, Y.; Xu, W.; Lapidus, S.; Wang, H.; He, X.; Chen, Z. In situ observation of thermal-driven degradation and safety concerns of lithiated graphite anode. *Nat. Commun.* **2021**, *12*, 4235. [[CrossRef](#)]
38. Shalnev, S.; Krzack, S.; Küster, F.; Friedrich, H.-J.; Meyer, B.; Gräßner, M. An experimental investigation into the conversion of nuclear graphite by oxygen and carbon dioxide: Kinetics and change in pore structure. *Fuel* **2024**, *357*, 129756. [[CrossRef](#)]
39. Yu, R.; Zeng, W.; Zhou, L.; Van Tendeloo, G.; Mai, L.; Yao, Z.; Wu, J. Layer-by-layer delithiation during lattice collapse as the origin of planar gliding and microcracking in Ni-rich cathodes. *Cell Rep. Phys. Sci.* **2023**, *4*, 101480. [[CrossRef](#)]
40. Rowden, B.; Garcia-Araez, N. A review of gas evolution in lithium ion batteries. *Energy Rep.* **2020**, *6*, 10–18. [[CrossRef](#)]

**Disclaimer/Publisher's Note:** The statements, opinions and data contained in all publications are solely those of the individual author(s) and contributor(s) and not of MDPI and/or the editor(s). MDPI and/or the editor(s) disclaim responsibility for any injury to people or property resulting from any ideas, methods, instructions or products referred to in the content.